Discover Oncology

RESEARCH Open Access

Multi-omics analysis reveals that CAPG positive macrophages are key immunosuppressive drivers and prognostic determinants in the ferroptosis landscape of hepatocellular carcinoma

Xisheng Yin[1,2,3], Yantong Li[1,2,3], Shi Zheng[1,2,3], Chunhui Pan[1,2,3], Zihan Tian[1,2,3] and Xiaolin Zhong[1,2,3*]

*Correspondence:
Xiaolin Zhong
zhongxl519@hotmail.com
[1]Department of Gastroenterology, The Affiliated Hospital of Southwest Medical University, Luzhou 646000, China
[2]The Public Platform of Advanced Detecting Instruments, Public Center of Experimental Technology, Southwest Medical University, Luzhou 646000, China
[3]Human Microecology and Precision Diagnosis and Treatment of Luzhou Key Laboratory, Luzhou 646000, China

Abstract

Hepatocellular carcinoma (HCC) is characterized by substantial heterogeneity and immune tolerance, and its therapeutic efficacy is profoundly influenced by the immune microenvironment. Ferroptosis, an iron-dependent form of regulated cell death, is closely linked to tumor immune regulation. We conducted an integrative multi-omics analysis to systematically delineate the composition and function of the ferroptosis–immunity network in HCC. Using TCGA data, we identified ferroptosis-related prognostic genes. By integrating these with immune features via weighted gene co-expression network analysis (WGCNA), we defined 55 ferroptosis–immune microenvironment–related genes (FIMRGs). Single-cell transcriptomic analysis showed that, among immune cell types, macrophages exhibited the highest ferroptosis–immunity activity. Spatial transcriptomics revealed that macrophages with high ferroptosis signaling (FehighMac) preferentially infiltrated tumor nests. These macrophages engaged in robust interactions with T cells via ligand–receptor axes such as ICAM1–ITGAX/ITGB2, TNF–TNFR, and LGALS9–CD45, potentially promoting T-cell exhaustion and shaping an immunosuppressive microenvironment. We identified CAPG-positive macrophages (CAPG + Mac) as the key driver of this process. Characterized by suppressed ferroptosis, enhanced glutathione metabolism, and upregulated immune checkpoints, CAPG + Mac appear to foster an immune-tolerant microenvironment. A prognostic model constructed from CAPG + Mac signature genes effectively stratified HCC patients into high- and low-risk groups and demonstrated stable predictive performance in external validation. This study reveals that CAPG + Mac putatively modulate ferroptosis signaling to influence immune homeostasis, highlighting them as a key target for HCC progression and immunotherapy responsiveness.

Keywords Hepatocellular carcinoma, Ferroptosis, CAPG positive macrophages, T cell exhaustion

1 Background

Hepatocellular carcinoma (HCC) remains a formidable global health challenge, ranking as the sixth most frequently diagnosed cancer and the third leading cause of cancer-related mortality in 2020. This stark mortality-to-incidence ratio underscores a dismal prognosis, with 5-year survival rates stagnating between 5% and 30% in most countries (https://doi.org/10.71321/e37ss652) [1]. The clinical management of HCC is com plicated by late-stage diagnosis, underlying liver pathologies, and high recurrence rates. Although the advent of immunotherapy has revolutionized the landscape for this historically chemotherapy-refractory malignancy, its clinical efficacy is frequently compromised by the heterogeneity of the tumor microenvironment (TME) [2,3,4]. Therefore, it remains an urgent priority to comprehensively elucidate the mechanisms of hepatocarcinogenesis to provide new perspectives for overcoming current therapeutic bottlenecks in HCC.

Ferroptosis is an iron-dependent form of cell death driven by the lethal accumulation of reactive oxygen species (ROS) that disrupt redox homeostasis, while glutathione peroxidase 4 (GPX4) serves a key protective role by mitigating lipid peroxidation [5,6]. Extensive evidence underscores the pivotal role of ferroptosis in cancer biology; tumor cells often suppress this pathway to sustain proliferative and invasive capacities [5]. Conversely, inducing ferroptosis has emerged as a promising strategy to inhibit tumor growth, enhance immunotherapeutic responses, and overcome drug resistance [7]. Building on this therapeutic potential, recent studies have explored specific ferroptosis-inducing strategies to optimize outcomes in HCC. For instance, targeting the novel ferroptosis suppressor S100P has been shown to effectively inhibit HCC tumorigenesis by remodeling lipid metabolism [8]. Similarly, modulating epigenetic and post-translational modifications offers a precision approach to reactivate silenced ferroptosis pathways, thereby suppressing tumor progression [9]. Notably, nanomedicine targeting xCT-mediated ferroptosis repolarizes macrophages to sensitize HCC to anti-PD-L1 immunotherapy, enhancing overall treatment efficacy [10].

Importantly, mounting evidence supports bidirectional crosstalk between ferroptosis and the TME. For example, CD8 + T cells promote lipid peroxidation and ferroptosis in tumors by secreting interferon-γ (IFN-γ), which downregulates SLC7A11 [11]. Ferroptotic cancer cells can also release immunostimulatory signals that drive dendritic cell maturation, increase macrophage phagocytosis of ferroptotic cells, and enhance CD8 + T-cell infiltration to activate antitumor immunity [12]. Moreover, triggering ferroptosis in immunosuppressive cells can bolster antitumor responses: M2-like tumor-associated macrophages (TAMs) suppress antitumor immunity, and inducing their ferroptosis can alleviate immunosuppression and improve immunotherapy efficacy [13,14]. Likewise, Treg-specific deletion of GPX4 induces ferroptosis in Treg cells and augments antitumor immunity [15]. Collectively, these findings underscore a complex interplay among ferroptosis, the TME, and antitumor immunity, and support ferroptosis as a viable avenue for cancer therapy.

However, the ways in which ferroptosis–immune interactions shape the initiation and progression of HCC remain incompletely defined. Accordingly, this study aims to identify genes linked to ferroptosis and immune cell infiltration in HCC, evaluate their prognostic significance and associated molecular mechanisms, deepen understanding of HCC pathogenesis, and provide new strategies for targeted therapy.

2 Materials and methods

2.1 Data sources

We obtained the TCGA-LIHC cohort from the Genomic Data Commons (GDC) portal (https://portal.gdc.cancer.gov/), comprising 374 HCC samples and 50 normal samples. To characterize the HCC tumor microenvironment, we downloaded the GSE235057 dataset from the Gene Expression Omnibus (GEO) (https://www.ncbi.nlm.nih.gov/gds), which includes 10 HCC tissue specimens and 10 matched adjacent non-tumor tissue samples. Spatial transcriptomics data for HCC were obtained from GSE224411 and generated by spatially resolved RNA sequencing using the 10x Genomics Visium platform. In addition, 167 ferroptosis-related genes were curated from the FerrDb database.

2.2 Identification of differentially expressed genes and unsupervised clustering

Differentially expressed genes (DEGs) between normal and HCC samples in the TCGA-LIHC cohort were identified using the limma R package [16] with thresholds of |log2 fold change| > 1 and adjusted $P < 0.05$. Intersecting these DEGs with the 167 ferroptosis-related genes defined the differentially expressed ferroptosis-related genes (DEFRGs). Prognosis-associated DEFRGs were identified using univariate Cox regression. Based on the expression of these genes, TCGA-LIHC samples were clustered with the partitioning around medoids (PAM) algorithm implemented in the ConsensusClusterPlus R package [17]. Gene set variation analysis (GSVA) was performed using the GSVA R package to assess differences in biological pathways among the ferroptosis subgroups.

2.3 Assessment of immune cell infiltration and weighted gene co-expression network analysis

To characterize the immune microenvironment in HCC samples, we compiled gene sets representing immune cell subtypes and immune features and applied single-sample gene set enrichment analysis (ssGSEA) [18] to quantify immune cell infiltration and immune feature scores for each HCC sample. The ssGSEA-derived metrics were treated as clinical traits. Using the Weighted Gene Co-expression Network Analysis (WGCNA) R package [19], we constructed a weighted co-expression network from the TCGA-LIHC expression matrix. Distinct modules were identified via dynamic tree cutting with a minimum module size of 100 genes, followed by merging of similar modules using a threshold of 0.45. We then evaluated correlations between these modules and immune cell infiltration, designating the module with the highest Pearson correlation as the key module. To further determine ferroptosis–immune microenvironment–related genes (FIMRGs) in HCC, we performed co-expression analysis between genes in the key module and the prognosis-related DEFRGs; genes with a correlation coefficient > 0.5 and $P < 0.05$ were defined as FIMRGs.

2.4 Single-cell sequencing data processing

For single-cell RNA-seq analysis, we performed quality control by removing cells with total transcripts (nCount_RNA) > 30,000, expressed features (nFeature_RNA) > 5,000, mitochondrial gene content > 15%, or hemoglobin gene content > 1%. Seurat (v4.3.0) was used for the standard workflow, including normalization, identification of variable genes, and scaling (NormalizeData, FindVariableFeatures, ScaleData), dimensionality reduction (RunUMAP, RunTSNE), and graph-based unsupervised clustering (FindNeighbors,

FindClusters). To correct batch effects between tumor and normal samples, we applied the Harmony R package [20]. Clustering results were visualized with t-SNE plots. Cell types were annotated using canonical marker genes, with visualization generated by the ComplexHeatmap R package. The ClusterGVis R package was used to examine trends in differentially expressed genes for each cell cluster and to perform functional annotation. We applied five algorithms—AddModuleScore, ssGSEA, AUCell, UCell, and singscore—to score single cells based on the FIMRGs derived from the co-expression analysis. This multi-algorithm strategy enhances robustness, mitigates errors and method-specific bias, and produces comprehensive, reliable, and biologically meaningful results. Using these scores, we quantified a ferroptosis–immune microenvironment score across cell types in tumor and normal groups. Macrophages were then stratified into two groups according to this score. Gene set enrichment within macrophage subpopulations was assessed using the fgsea R package. To investigate intercellular communication dynamics between macrophage subgroups and other cell types, we used the CellChat R package [21] to infer overall, pathway-level, and gene-level communication probabilities, with circle and chord diagrams for visualization. Finally, macrophage developmental trajectories were inferred using the VECTOR algorithm, which identifies starting cells in an unsupervised manner and computes directional developmental vectors based on network distances from starting cells within the UMAP embedding [22].

2.5 Processing of spatial transcriptomics data

Spatial transcriptomics data were processed and analyzed using the Seurat package. We applied SCTransform to normalize and scale UMI counts and to identify the most variable features. Dimensionality reduction was performed with RunPCA to simplify the data structure. SpatialFeaturePlot was used for post-reduction and clustering visualization, allowing us to display the spatial distribution of cell subpopulations within tissue sections and gain deeper insights into spatial organization and functional states.

To explore cellular metabolic characteristics, we used the scMetabolism R package and the VISION algorithm to score each cell and determine pathway activity. This detailed metabolic analysis reveals complex intracellular functions and dynamics, providing both spatial and functional perspectives on tumors and thereby deepening our understanding of tumor complexity.

To uncover biological processes across whole tissues and resolve the spatiotemporal evolution of malignancy, we used stLearn to infer spatial developmental trajectories. This analysis leverages PAGA trajectory analysis based on tissue-wide, SME-normalized gene expression data to reveal connections within subclusters [23].

2.6 Spatial distribution of cell subtypes defined by single-cell sequencing data

Deconvolution analysis is used to estimate cell-type proportions within heterogeneous samples, and accuracy is improved by integrating single-cell and spatial transcriptomics datasets. scRNA-seq reveals cellular diversity within tissues, while spatial transcriptomics precisely maps the locations of these cells, capturing spatial complexity. Using robust cell type decomposition (RCTD), we mapped cell types identified in the reference scRNA-seq dataset onto spatial transcriptomics data [24].

2.7 Exploration of spatial interaction patterns in HCC

Based on RCTD deconvolution results, we performed colocalization analysis of spatially resolved cells using the mistyR R package [25]. MistyR is an interpretable machine learning framework for knowledge extraction and analysis from single-cell, highly multiplexed, spatially resolved data. It primarily analyzes intra- and intercellular relationships to capture short- and long-range cell–cell interactions. By integrating spatial transcriptomics data with deconvolution analysis, we systematically revealed spatial relationships among cell types. We first conducted kNN analysis to compute the six nearest neighbors for each spot and selected CAPG + Mac and CAPG negative macrophages(CAPG-Mac). Based on these spots, we constructed a spatial network. We then calculated node degrees for each spot to generate a homotypic cell interaction network, visually presenting the spatial distribution and interrelationships of CAPG + Mac and CAPG-Mac. Furthermore, we examined the spatial distribution between CAPG + Mac and CD8 + T cells, CD4 + T cells, and resting T cells to generate a heterotypic cell interaction network. These networks demonstrate the spatial distribution of various cell types and reveal their intricate interrelationships, providing important insights into spatial cell–cell interactions [26].

2.8 Identification and spatial validation of cell communication pathways

To elucidate key communication pathways between CAPG + Mac and T cells, we employed the "CommPath" R package to identify crucial ligand-receptor pairs [27], which were then annotated using the KEGG database for associated pathways. Pathway activation scores were subsequently calculated via the UCell method. Significantly upregulated pathways in each cell cluster were identified from these scores, with the top ten selected for heatmap visualization. An intercellular communication map, formatted as "upstream cell - receptor center - ligand - downstream cell," was constructed, designating CAPG + Mac as the upstream and T cells as the downstream cells. Furthermore, the SpaGene system was utilized to analyze spatially variable genes and receptor-ligand interactions, verifying the spatial co-localization of these pairs [28].

2.9 Construction and validation of a survival prediction model based on CAPG + Mac marker genes

In the filtered single-cell dataset, we used FindMarkers to identify differentially expressed genes associated with CAPG + Mac (logFC = 0.6). We selected the TCGA dataset ($n = 368$) as the training set and the ICGC dataset ($n = 240$) as the external validation set. First, univariate Cox regression analysis was performed to assess associations between genes and survival prognosis. To further identify key genes, we applied Lasso regression and selected the optimal model via ten-fold cross-validation of the penalty parameter λ, thereby achieving feature selection while reducing multicollinearity and yielding a set of candidate genes with stable predictive power. Based on the Lasso results, we constructed a multivariable Cox regression model to identify optimal feature genes. The Cox model derived from the training set was then applied to predict survival in the validation set. Kaplan–Meier survival curves were generated using the survival package, and time-dependent Receiver Operating Characteristic Curve (ROC) curves were plotted using the timeROC package to evaluate predictive accuracy. In addition, univariate and multivariate Cox regression analyses were conducted to assess the effects of clinical

factors (age, T stage, N stage, M stage, stage, and risk score) on survival in HCC patients. Finally, we explored the protein expression of the model genes on the Human Protein Atlas (HPA) database.

2.10 Integrated analysis of risk scores with the immune microenvironment and immune-related pathways

To investigate the immune landscape in HCC, we used the MCPcounter method to quantify the relative abundance of various immune cell types within the tumor microenvironment. In addition, we applied the ESTIMATE method to calculate immune scores and tumor purity, helping to clarify how the immune microenvironment influences patient survival outcomes. Furthermore, we performed ssGSEA to evaluate activation levels of different biological pathways in HCC samples, highlighting the importance of immune-related pathways in survival prognosis. Finally, we identified key checkpoint genes and used density plots to illustrate differences in their expression between high-risk and low-risk cohorts. We further evaluated the potential of the model to assess the immune treatment response in the immune treatment datasets GSE78220 [29], GSE135222, and GSE91061 [30].

2.11 Statistical analysis

In this study, logarithmic transformation and batch correction were used to standardize the data. All analyses and visualizations were conducted using R software (version 4.3.1) and Python software (version 3.9). A series of statistical methods were used to develop predictive models, including univariate, lasso and multivariate Cox regression analyses. For statistical comparison, t-test was used to evaluate the differences between the two groups, and one-way analysis of variance was used to evaluate the differences among multiple groups. The Wilcoxon test is explicitly used to compare the high-risk group with the low-risk group. Statistical significance is defined as a p value less than 0.05, and the significance levels are expressed as follows: * ($p < 0.05$), ** ($p < 0.01$), and *** ($p < 0.001$).

3 Results

3.1 Identification of ferroptosis-related subtypes in HCC

To identify DEFRGs between HCC and normal samples, we first screened DEGs in the TCGA-LIHC cohort by comparing HCC with normal tissues. As shown in Fig. 1A, 5,622 DEGs were identified, including 2,462 upregulated and 3,160 downregulated genes. The top 100 DEGs are shown in Fig. 1B. We then intersected these 5,622 DEGs with 167 ferroptosis-related genes (FRGs), yielding 36 DEFRGs (Fig. 1C). Next, we performed univariate Cox regression analysis on these 36 genes to assess their associations with overall survival (OS) in HCC patients and identified 15 genes significantly associated with OS ($p < 0.05$): STMN1, MAFG, TXNIP, SLC7A11, RRM2, PCK2, MT3, IL33, HMOX1, GPT2, CBS, CAPG, AURKA, ASNS, and ALB (Fig. 1D). Pearson correlation analysis among the 15 genes revealed positive correlations for STMN1–RRM2, STMN1–AURKA, SLC7A11–MAFG, RRM2–AURKA, PCK2–GPT2, and PCK2–ALB (Fig. 1E). To further explore potential interactions among the encoded proteins, we constructed a protein–protein interaction (PPI) network comprising 13 nodes and 16 edges (Fig. 1F), suggesting possible synergistic relationships. To identify ferroptosis-related

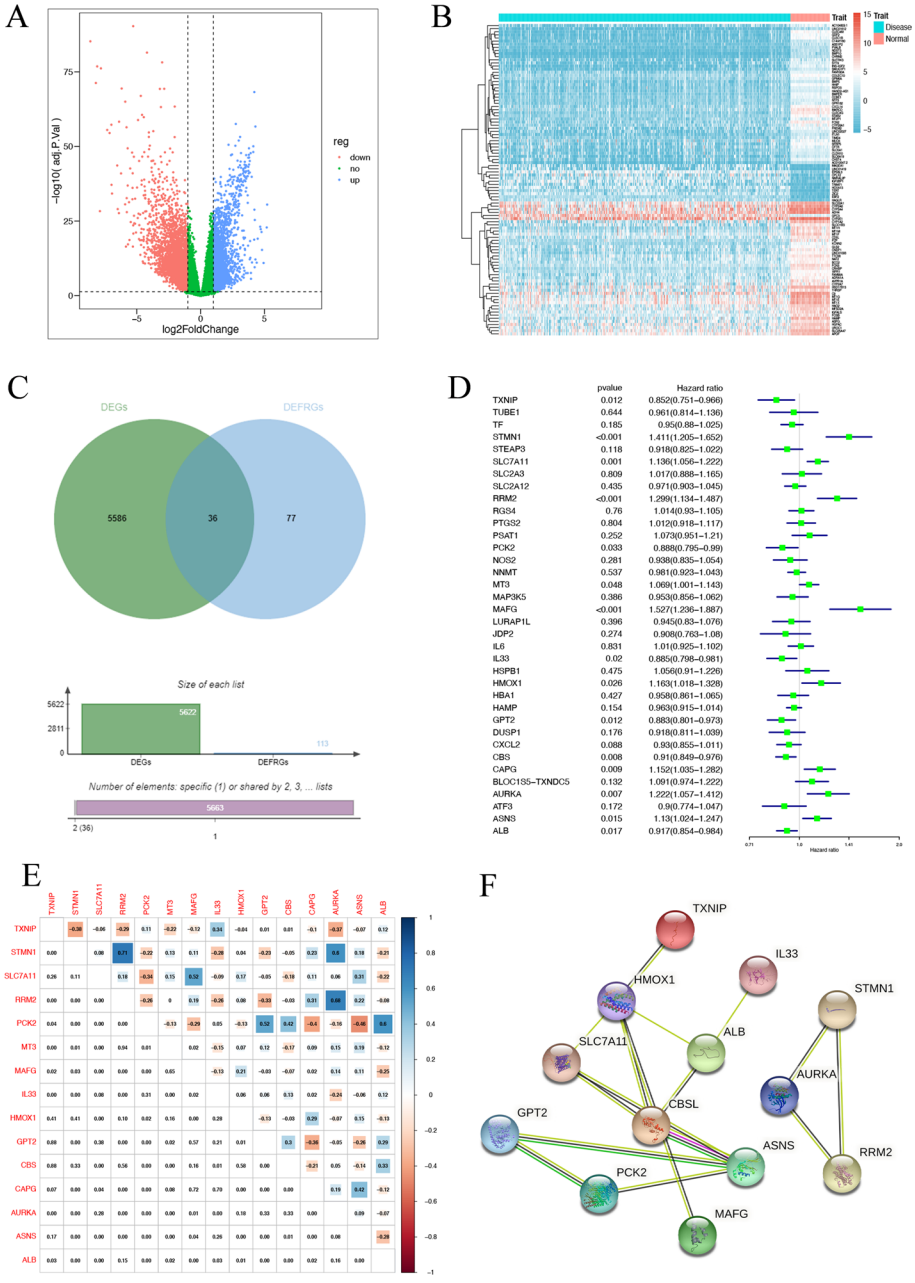

Fig. 1 A screen of prognosis-related differential ferroptosis genes (DEFRGs) in hepatocellular carcinoma (HCC). (**A**) Volcano plot of differential expressed genes (DEGs) between the normal and HCC groups. The up-and down-regulated DEGs are respectively highlighted in blue and red. (**B**) Expression profiles of the top 100 DEGs. (**C**) Venn diagram of DEFRGs. (**D**) DEFRGs significantly correlated with HCC prognosis. (**E**) Heat map of correlation between prognostic DEFRGs. (**F**) Protein-protein interaction network of prognostic DEFRGs.

HCC subtypes, we performed unsupervised clustering of 370 HCC samples based on the expression of the 15 OS-associated DEFRGs, defining two subtypes: Cluster 1 ($n = 140$) and Cluster 2 ($n = 230$) (Supplementary Fig. 1A). Survival analysis indicated a significant prognostic difference between the two subtypes, with Cluster 2 exhibiting a survival advantage (Supplementary Fig. 1B). To investigate potential mechanisms underlying these differences, we conducted immune infiltration profiling and Kyoto Encyclopedia of Genes and Genomes (KEGG) enrichment analyses to compare functional and signaling

pathways between subtypes. Most immune cell and immune feature enrichment scores were higher in Cluster 1 than in Cluster 2 (Supplementary Fig. 1C), and correlations among immune cells and immune features are shown in Fig. 2E. Additionally, Cluster 1 was significantly enriched for multiple oncogenic pathways such as the p53 signaling pathway and certain metabolic pathways, whereas Cluster 2 was mainly enriched for glucose metabolism and immune-related pathways, including the PPAR signaling pathway and the adipocytokine signaling pathway. These pathway-level differences may underlie the poorer prognosis of Cluster 1 and indicate that ferroptosis-based molecular subtyping captures tumor heterogeneity (Supplementary Fig. 1D). Supplementary Fig. 1E depicts correlations among different immune cells and immune features.

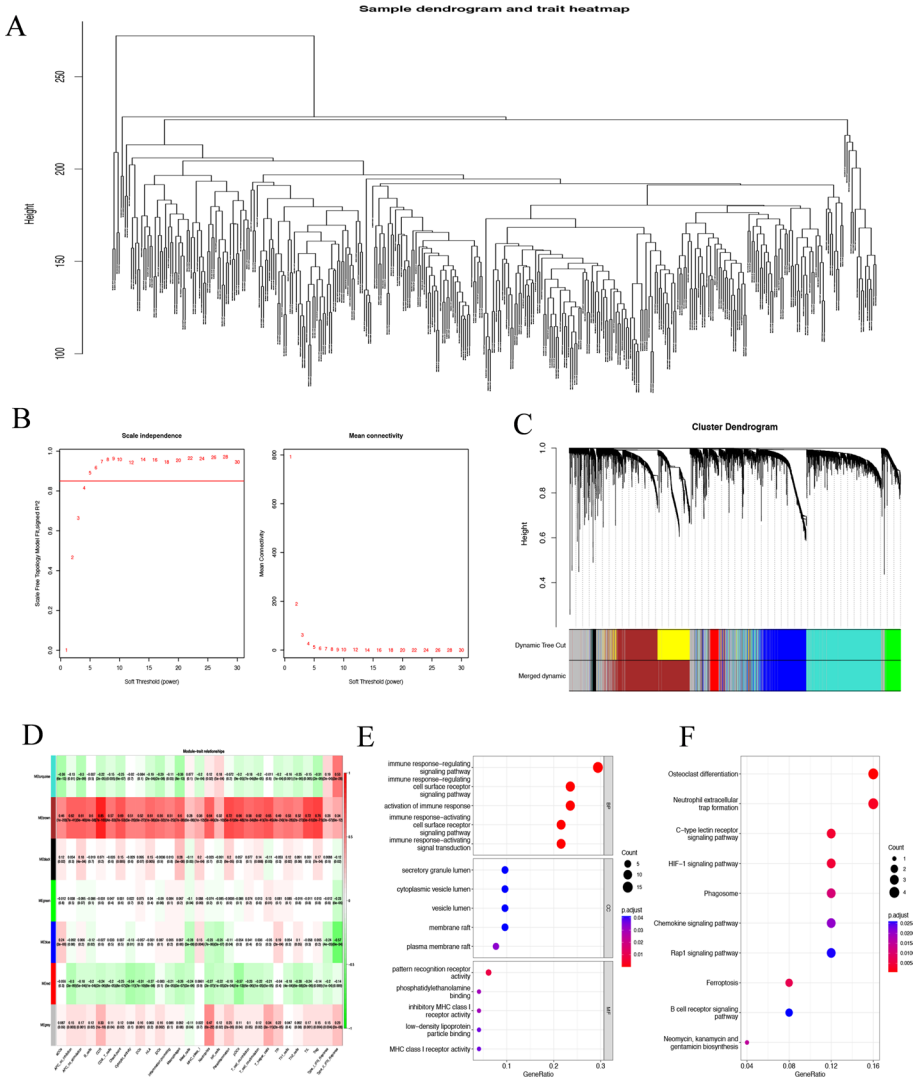

Fig. 2 WGCNA analysis. (**A**) Cluster dendrogram of 370 samples. (**B**) The scale-free fit index for soft-thresholding powers. (**C**) Hierarchical clustering dendrogram of identified co-expressed genes in modules in HCC. Each colored row represents a color-coded module that contains a set of highly connected genes. A total of 7 modules was identified in HCC. (**D**) A heat map showing correlations between the gene modules and immune signature. Enrichment results for the top five GO (**E**) and top ten KEGG (**F**) of ferroptosis-immune microenvironment-related genes (FIMRGs).

3.2 Selection of FIMRGs

To further explore genes associated with the immune microenvironment, we incorporated infiltrating immune cells and immune feature metrics into WGCNA. No obvious outlier samples were observed in the clustering analysis (Fig. 2A). In soft-threshold selection, a power of 5 was chosen as optimal, yielding a scale-free topology fit index R^2 of 0.85 (Fig. 2B). Based on this power, we applied dynamic tree cutting for module detection and merged similar modules, resulting in seven co-expression modules (Fig. 2C). We then calculated correlations between each module and immune features (Fig. 2D) and found that the brown module had the strongest positive correlation with immune features. We therefore designated it as the key module, comprising 1,436 genes considered closely related to the immune microenvironment. To identify FIMRGs representative of HCC, we computed Pearson correlation coefficients between these 1,436 genes and the 15 prognosis-related DEFRGs. Using thresholds of correlation coefficient > 0.5 and $p < 0.05$, we extracted and de-duplicated the qualifying genes, obtaining 55 key FIMRGs (Supplementary Table 1). To gain insight into the functions and pathways of FIMRGs, we performed Gene Ontology (GO) and KEGG enrichment analyses. GO analysis yielded 291 enriched terms, including 279 biological process (BP), 7 cellular component (CC), and 5 molecular function (MF) terms (Supplementary Table 2). The top five entries for each category are shown in Fig. 2E. These genes were mainly enriched in "regulation of immune response signaling pathway," "regulation of immune response–activating cell surface receptor signaling pathway," "immune response activation," "immune response–activating cell surface receptor signaling pathway," and "immune response–activating signal transduction." In KEGG analysis, FIMRGs were primarily involved in 10 significant pathways, including "osteoclast differentiation," "neutrophil extracellular trap formation," "C-type lectin receptor signaling pathway," "HIF-1 signaling pathway," "ferroptosis," "phagosome," "chemokine signaling pathway," "Rap1 signaling pathway," and "B cell receptor signaling pathway" (Fig. 2F).

3.3 Single-cell transcriptomics reveals a key role for macrophages in FIMRG-mediated ferroptosis–immune functions

We next performed single-cell RNA-seq analysis to resolve cellular populations within the HCC microenvironment. Dimensionality reduction and clustering divided cells into 38 distinct clusters (Fig. 3A). Using known marker genes, we annotated major immune and stromal cell types, including B cells, CD4 + T cells, CD8 + T cells, conventional T cells, endothelial cells, fibroblasts, hepatocytes, macrophages, mast cells, NK cells, and plasma cells (Fig. 3B). Cluster-specific marker genes are shown in Fig. 3C. We also conducted differential expression and GO enrichment analyses for each cell subset (Fig. 3D). The DEGs of each subset were significantly enriched in corresponding biological functions and pathways, supporting the accuracy and biological plausibility of our annotations. Using the 55 FIMRGs, we scored the single-cell dataset with five methods—AUCell, UCell, singscore, GSVA, and AddModuleScore. Integrating these approaches revealed notable patterns: macrophages exhibited markedly higher ferroptosis–immune scores than other cell subsets (Fig. 3E). Figure 3F shows the distribution of ferroptosis–immune scores across cells stratified by tissue type. These findings suggest that macrophages may play a central role in ferroptosis–immune microenvironment–related functions.

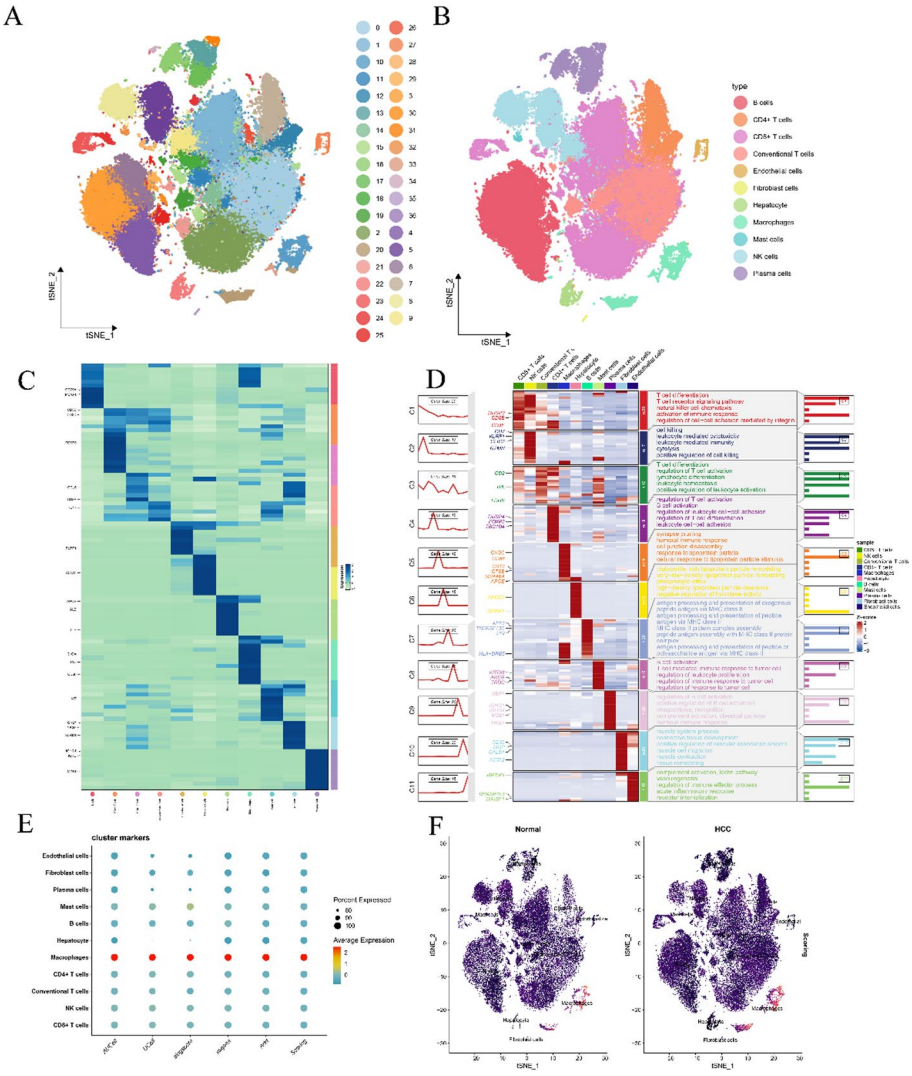

Fig. 3 Classification of cell subpopulations in HCC and enrichment scores of FIMRGs. (**A**) The t-SNE graph shows 37 clusters obtained after dimensionality reduction and clustering based on the GSE235057 dataset. (**B**) Based on the cell marker genes, 11 types of cell subpopulations were annotated. (**C**) The heat map shows the marker genes of each cell subpopulation. (**D**) The heat map shows the biological entries for the enrichment of marker genes in each cell subpopulation. (**E**) The bubble plot shows the enrichment fraction of FIMRGs for each cell type in HCC. (**F**) The t-SNE plot facets showed the enrichment scores of FIMRGs in the Normal group and the HCC group.

3.4 Spatial transcriptomics identifies ferroptosis-related metabolic pathway activity and infers intratumoral spatial trajectories in HCC

To further explore the spatial distribution of ferroptosis signaling and tumor evolutionary trajectories, we integrated spatial transcriptomic data to examine the expression patterns of ferroptosis-related metabolic pathways within tissue space and their potential trends of change. Quality control results for the spatial transcriptomics data are shown Fig. 4A. After dimensionality reduction and clustering, eight cell subpopulations were obtained (Fig. 4B, C). To investigate ferroptosis-related metabolic pathway activity in HCC cells, we assessed metabolic activity using the scMetabolism R package. Cluster 1 exhibited more active glycerophospholipid metabolism with relatively lower glutathione metabolism, whereas cluster 3 showed the inverse pattern (Fig. 4D). Figure 4E and F display the spatial activity distributions of glycerophospholipid metabolism and glutathione

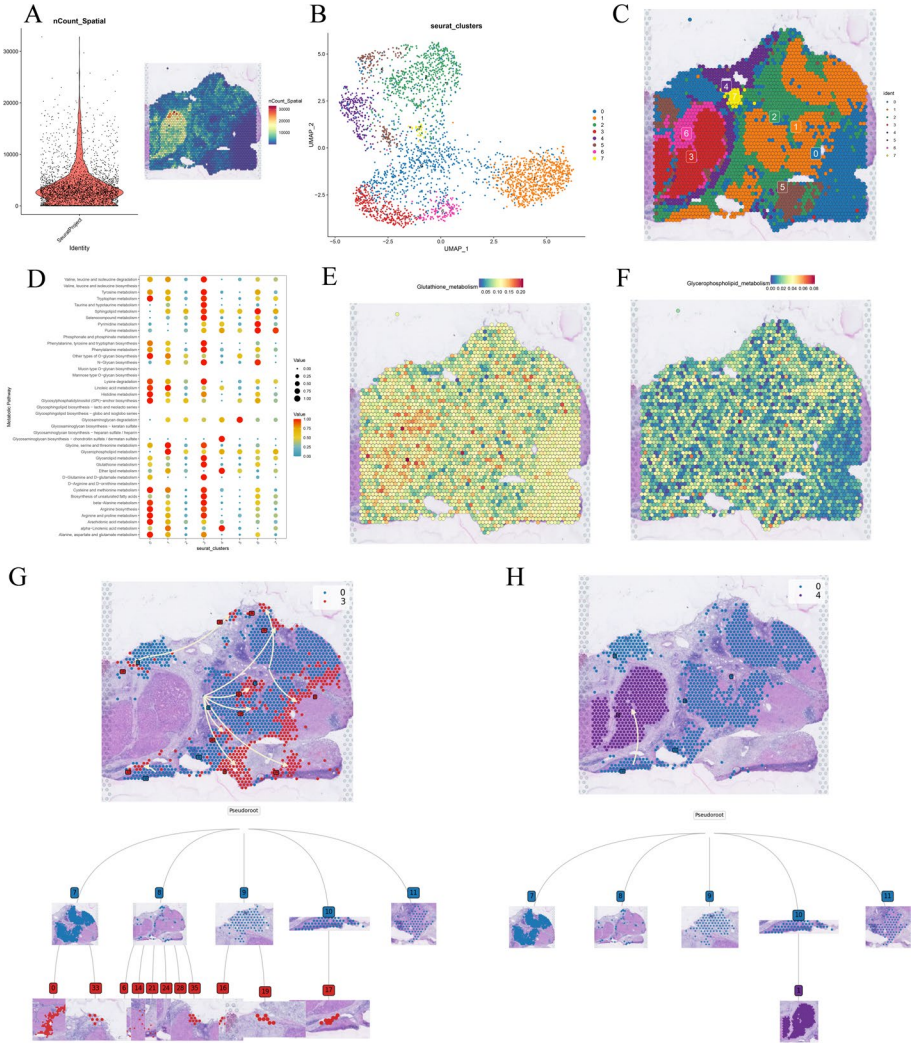

Fig. 4 Spatial distribution and trajectory inference of ferroptosis-related signals. (**A**) Spatial feature visualization showing the total gene counts per spatial spot and their distribution across the tissue section. (**B**) UMAP plot illustrating the clustering of spatial transcriptomic spots based on gene expression profiles. (**C**) Spatial mapping of the identified clusters across the tissue section. (**D**) Bubble plot showing the activity of metabolism-related pathways in different spatial clusters. (**E**–**F**) Spatial enrichment analysis of glutathione metabolism and glycosphingolipid metabolism pathways. (**G**–**H**) Spatial trajectory inference depicting the potential progression routes of ferroptosis-related signals, with arrows indicating the inferred spatial transitions between regions.

metabolism. Under both global and local paradigms of spatial trajectory inference, we applied the stLearn algorithm to decipher spatial evolutionary trajectories and complex transcriptional connectivity among subclones within HCC. Our analyses suggest that the directional spatial trajectory of tumor cells originates in regions with reduced glutathione activity and ultimately peaks in regions characterized by elevated glutathione metabolism (Fig. 4G). Moreover, glycerophospholipid metabolic activity decreased along tumor evolution (Fig. 4H). This relationship indicates that the evolutionary trajectory of HCC subclones begins with subclones exhibiting high ferroptosis activity and, over time, progresses toward subclones with reduced ferroptosis signaling.

3.5 Ferroptosis–immune signaling shapes macrophage spatial localization and functional differentiation

Given that macrophages display more active ferroptosis–immune signaling than other cellular subpopulations, we further investigated its impact on macrophage function. We extracted tumor-derived macrophages and reclustered them into 14 cellular subpopulations (Fig. 5A). A density plot depicts the distribution of ferroptosis–immune scores (Fig. 5B). Combined with pseudotime analysis, macrophage ferroptosis–immune scores showed an upward trend along the tumor evolutionary trajectory (Fig. 5C). To assess the influence of ferroptosis–immune signaling on spatial distribution, we stratified macrophages into a high ferroptosis signaling group (FehighMac) and a low ferroptosis signaling group (FelowMac) based on the median score.

Using RCTD, we integrated scRNA-seq with spatial transcriptomics and visualized FehighMac and FelowMac across tissue sections. FehighMac preferentially infiltrated

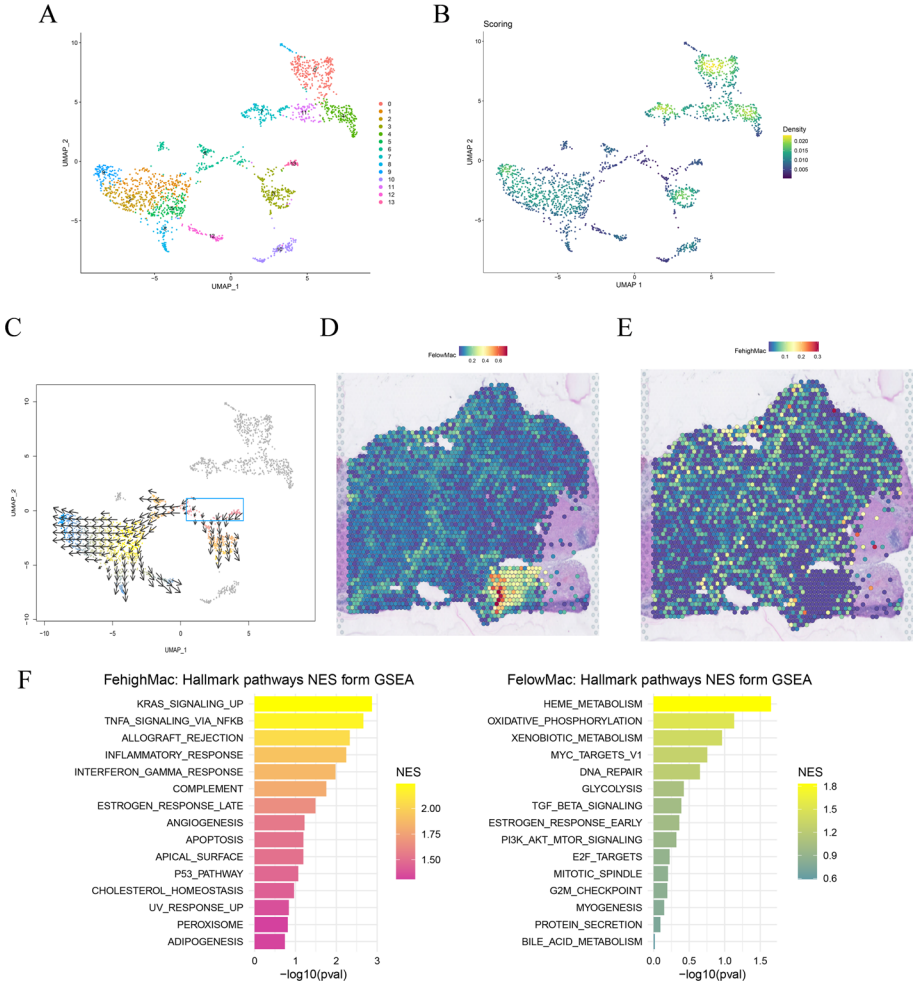

Fig. 5 Pseudo-temporal analysis of macrophage subsets and spatial localization of different iron poisoning-related macrophage states identified by RCTD. (**A**) UMAP visualization of macrophage subclusters based on single-cell transcriptomic profiles. (**B**) Density distribution of enrichment scores for ferroptosis-related immune-modulating genes (FIMRGs) across macrophage subclusters. (**C**) Pseudotime trajectory inference indicating the differentiation direction of macrophage subpopulations (arrow direction). (**D–E**) Spatial mapping of macrophages with high (FehighMac) and low (FelowMac) ferroptosis signatures in tissue sections. (**F**) Gene Set Enrichment Analysis (GSEA) highlighting the hallmark pathways enriched in FehighMac and FelowMac populations, illustrating their distinct biological functions.

tumor nests, whereas FelowMac mainly accumulated at tumor edges (Fig. 5D, E). Pathway enrichment analysis indicated that FehighMac was significantly enriched for inflammation-related pathways (TNF-α, IFN-γ), while FelowMac was primarily enriched for metabolic pathways, including heme and xenobiotic metabolism (Fig. 5F). These results suggest a close link between ferroptosis–immune signaling and both the spatial localization and functional states of macrophages.

3.6 Cell-cell communication analysis reveals a potential association between fehighmac and T cell exhaustion

Recent single-cell multi-omics studies indicate that immunosuppressive communication along the myeloid–T cell axis is pivotal in driving T cell exhaustion and immunotherapy resistance within the TME. Whether macrophages with enhanced ferroptosis signaling participate in this process and through which mechanisms remains unclear. We therefore dissected immunosuppressive communication mediated by FehighMac, focusing on ligand–receptor networks between FehighMac and T cell subsets. In the ICAM network, FehighMac exhibited stronger communication toward CD8+, CD4+, and resting T cells than FelowMac (Fig. 6A). Prior work shows that adhesion pathways stabilize immunological synapses and prolong cell–cell contact via ICAM-1 (CD54) and LFA-1 (ITGAL/ITGB2), amplifying persistent TCR signaling and synergizing with inhibitory axes to weaken effector function [31, 32]. Consistently, in breast cancer models, tumor-derived PGRN remodeled TAM phenotypes, upregulated ICAM-1 on TAMs, and promoted adhesion to CD8 + T cells, reducing activation markers (IFNγ, CD69) and impairing CD8 + T cell function [33].

We also observed TNF–TNFRSF1A interactions from FehighMac to CD4 + and CD8 + T cells (Fig. 6B). Sustained TNF/TNFR signaling, together with adhesion molecule–mediated synapse stabilization, can foster a chronic inflammatory TME that promotes T cell functional decline and consolidates exhaustion [34]. Additionally, CD86 signaling was enriched between FehighMac and T cells (Fig. 6C). Single-cell analyses in classical Hodgkin lymphoma revealed high CD86 expression in TAMs that biases the CD86–CTLA-4 inhibitory axis, directly driving T cell exhaustion; targeting CD86 reverses immunosuppression with in vitro and in vivo efficacy [35]. Moreover, GALECTIN signaling substantially contributed to FehighMac–T cell communication (Fig. 6D). The LGALS9 (Galectin-9)–TIM-3 (HAVCR2) axis has been repeatedly implicated in CD8 + T cell exhaustion; LGALS9 binding to TIM-3 forms a glycan-dependent complex with PD-1, modulating T cell suppression and disease progression, and blockade can enhance anti–PD-1 efficacy [36, 37, 38, 39].

We next explored the potential association between FehighMac and immunosuppressive features. Checkpoint molecules were broadly expressed across lymphocyte clusters (Fig. 6E), including TIGIT, PDCD1 (PD-1), LAG3 (LAG-3), and CTLA4 (CTLA-4). Using TCGA HCC RNA-seq data, we computed a composite immune checkpoint score (TIGIT, PDCD1, LAG3, CTLA4) together with the top 15 FehighMac markers. The checkpoint signature score correlated closely with FehighMac markers ($p < 0.001$, $R = 0.496$) (Fig. 6F), suggesting that FehighMac may promote T cell exhaustion in the TME. Furthermore, TIDE analysis, which integrates features of T cell dysfunction and exclusion to predict immunotherapy response [40], showed that patients with high FehighMac scores had higher TIDE scores and were more likely to be resistant to

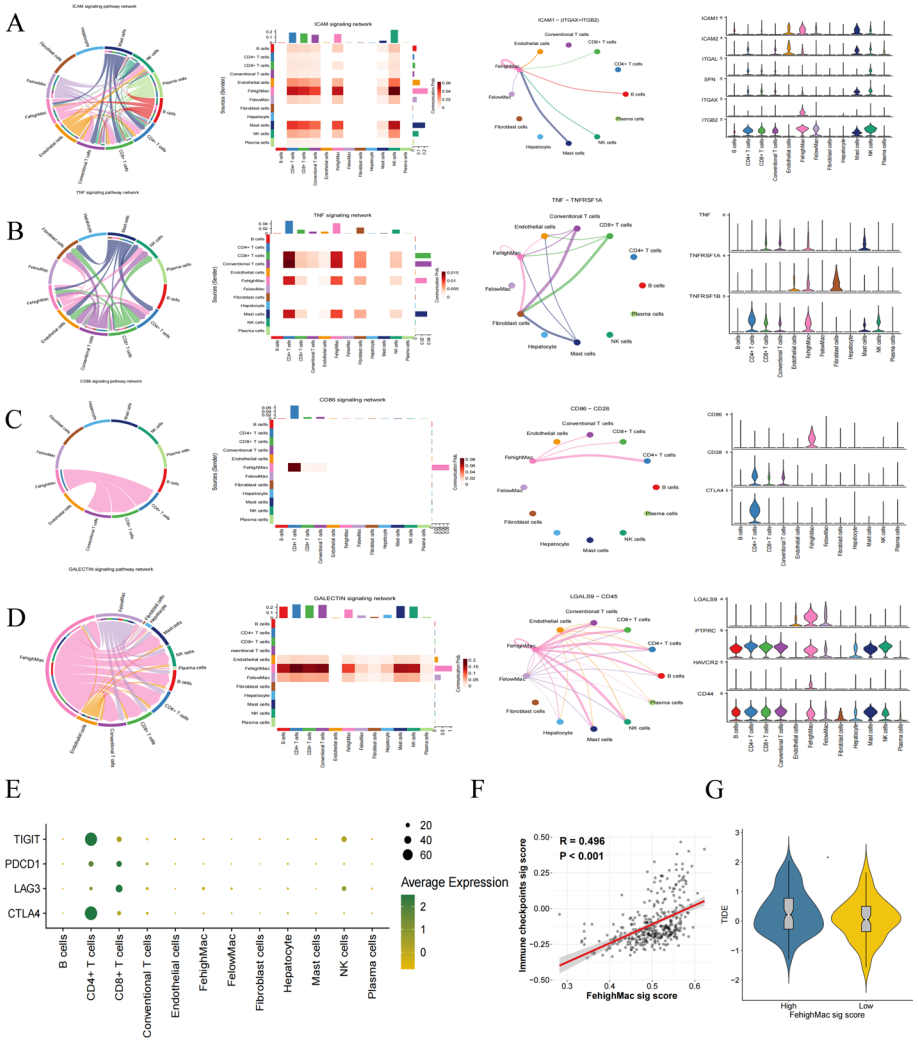

Fig. 6 FehighMac cellular communication with T cells forms the immunosuppressive landscape. (**A–D**) Chord diagrams, heatmaps, network plots, and violin plots illustrate significant interaction pathways and communication probabilities between macrophages with different ferroptosis signals and T cells via the ICAM, TNF, CD86, and GALECTIN signaling axes. The chord and violin plots show representative ligand–receptor pairs and their expression patterns across corresponding cell clusters. (**E**) Bubble plot showing the expression of T-cell exhaustion markers across clusters in the HCC single-cell dataset. (**F**) Scatter plot displaying a positive correlation between FehighMac signature scores and immune checkpoint enrichment scores ($R = 0.496$, $P < 0.001$). (**G**) Violin plot showing higher tumor immune dysfunction and exclusion (TIDE) scores in samples with high FehighMac signatures, indicating the presence of an immunosuppressive microenvironment.

immunotherapy than those with low scores (Fig. 6G). Together, these data indicate that FehighMac may play a crucial role in T cell suppression and suggest that ferroptosis-driven macrophage–T cell communication is likely involved in shaping an immunosuppressive microenvironment.

3.7 CAPG + Mac may reduce ferroptosis signaling by inducing T cell exhaustion, thereby promoting tumor progression

To identify key molecules underlying changes in macrophage ferroptosis signaling, we screened differentially expressed genes within macrophages and intersected them with FIMRGs to obtain macrophage-related FIMRGs. t-SNE visualizations show their distribution across cellular populations (Fig. 7A). FABP5, TREM2, and CAPG were

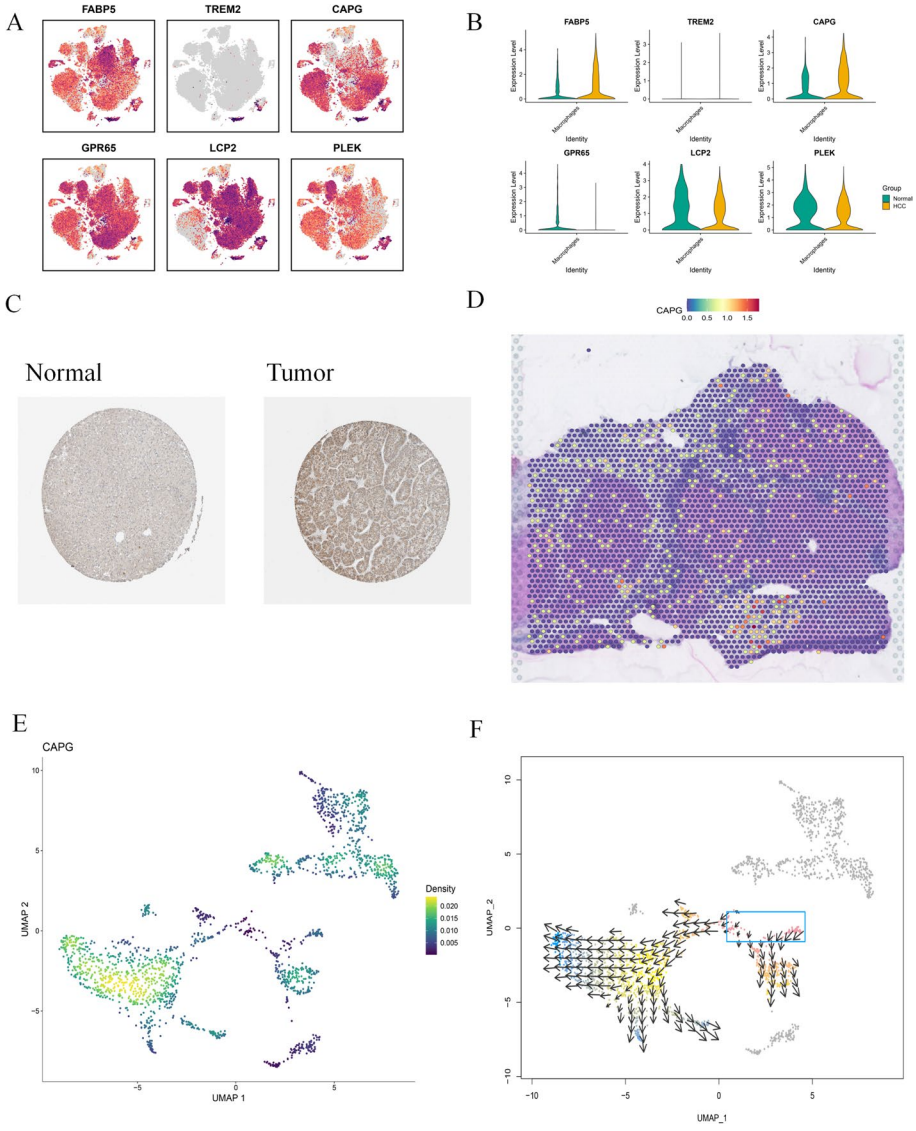

Fig. 7 Macrophage-specific CAPG expression derived from FIMRGs and its spatiotemporal characteristics. (**A**) UMAP visualization showing key genes (FABP5, TREM2, CAPG, GPR65, LCP2, and PLEK) identified from the intersection of macrophage-specific DEGs and FIMRGs. (**B**) Violin plots illustrating gene expression across different groups, with CAPG upregulated in the HCC group. (**C**) The immunohistochemical results showed that CAPG was expressed at a higher level in the HCC sample tissues. (**D**) Spatial transcriptomic map demonstrating the spatial distribution of CAPG expression within the tissue section. (**E–F**) UMAP and pseudotime analyses indicating that CAPG expression initially increases and then decreases along the macrophage differentiation trajectory.

highly expressed in tumor macrophages, whereas GPR65, LCP2, and PLEK were lower in tumor macrophages. Notably, CAPG showed abnormally high average expression in mast cells and macrophages (Fig. 7B). Furthermore, based on the immunohistochemical sections from the HPA database, we compared healthy liver tissues with liver cancer tissues. We found that the presence rate of CAPG in tumors was increased (Fig. 7C). We therefore focused on CAPG to probe its potential role in liver cancer immunity and macrophage function. Spatial maps display CAPG expression patterns in HCC sections (Fig. 7D), revealing pronounced spatial heterogeneity: lower levels in tumor nests and relatively higher expression in stromal regions. Pseudotime analysis suggested a peak in CAPG expression during mid-stage tumor progression.

To further assess CAPG's impact on macrophage function, we analyzed CAPG + Mac and CAPG-Mac within HCC sections (Fig. 8A–D). Most CAPG + Mac were located in the tumor stroma, whereas CAPG – Mac more frequently infiltrated tumor nest regions. Homotypic cell network maps delineated the spatial adjacency of CAPG + Mac and CAPG – Mac, clarifying intercellular interactions and tissue architecture. We then examined cell–cell communication between CAPG + Mac/CAPG – Mac and T cells. Heatmaps showed that CAPG + Mac–T cell interactions centered on HLA-mediated signaling, accompanied by dense IFN-γ/TNF inflammatory signaling and alternative checkpoints such as HLA-E/F, with the strongest signatures in CD8 + T cells (Fig. 8E–G). These observations align with prior studies: in solid tumors, the nonclassical HLA-E–NKG2A axis restricts CD8 + T cell effector function, and blockade can partially restore activity [41, 42]. In HBV-related HCC, HLA-DR+ tumor cells are associated with

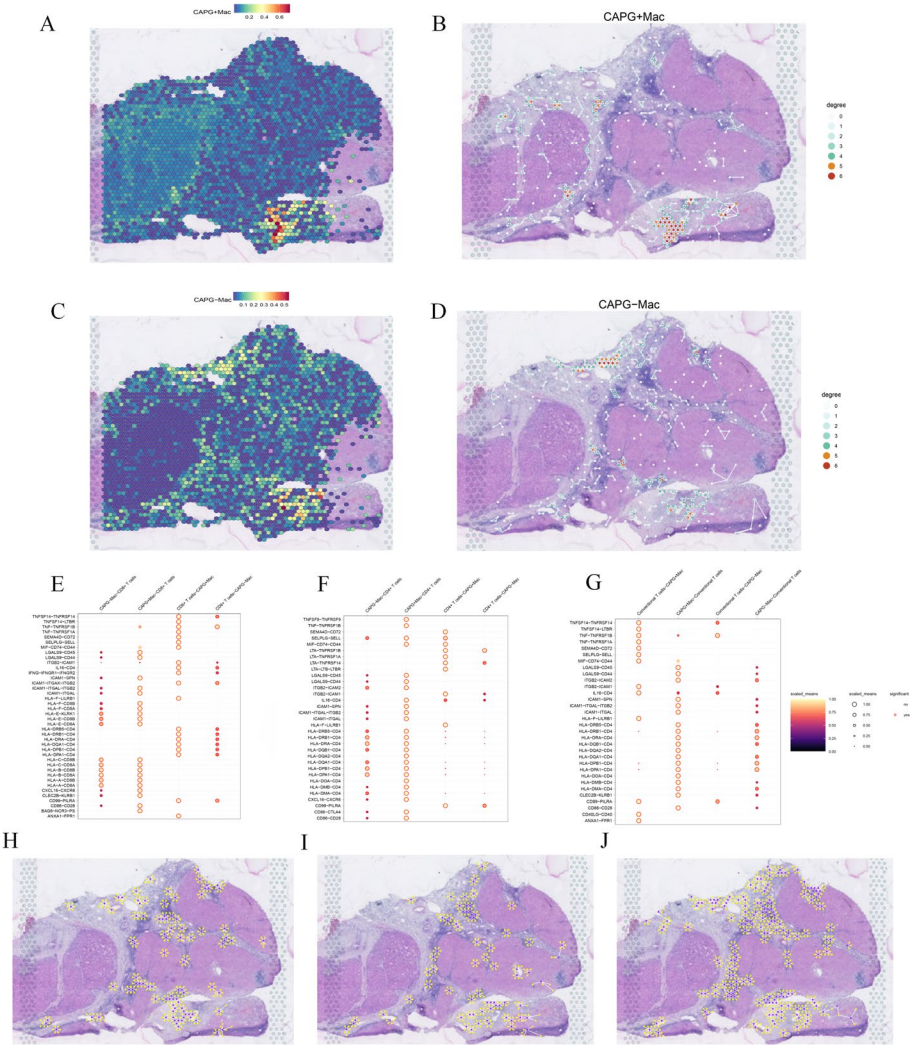

Fig. 8 Spatial distribution and intercellular communication networks of CAPG + Mac and CAPG-Mac. (**A**, **C**) Spatial transcriptomic maps showing the localization of CAPG + Mac and CAPG-Mac within tumor sections. (**B**, **D**) Homotypic cell-interaction networks of different macrophage subsets. (**E–G**) Bubble plots showing major ligand–receptor interactions between CAPG+ / CAPG– macrophages and CD8 + T cells, CD4 + T cells, and Conventional T cells, revealing key immunoregulatory signaling pathways. (**H–J**) Spatial mapping illustrating heterotypic interaction networks between CAPG + Mac and CD8 + T cells (**H**), CD4 + T cells (**I**), and Conventional T cells (**J**), highlighting distinct immune-cell distribution patterns within specific tumor regions.

CD8 + T cell exhaustion, linking aberrant antigen presentation to exhaustion [43]. In clinical TCR-T therapy, upregulated IFN-γ/antigen-presenting pathways coincide with enhanced inhibitory checkpoints, reflecting adaptive immunosuppression [44]. Cross-tumor evidence indicates that aberrant antigen presentation coexists with T cell exhaustion/immunosuppressive pathways as a common immune evasion feature [45,46].

At the spatial transcriptomics level, we constructed a heterotypic cellular network between CAPG + Mac and T cells. Analyses revealed tight proximity and an "encapsulation-like" arrangement of CAPG + Mac around T cells within stromal regions (Fig. 8H–J). This enveloping organization creates a critical node in the HCC immune ecology, facilitating close cell–cell communication and suggesting a local niche unfavorable to T cells, thereby limiting antitumor activity. MistyR-based analyses of juxta and para spatial modes likewise showed significant colocalization between CAPG + Mac and CD8 + T cells (Supplementary Fig. 2). Collectively, these results support a protumor role for CAPG + Mac in HCC progression.

3.8 Identification and spatial validation of potential communication pathways between CAPG + Mac and T cells

To explore the communication chain between CAPG + Mac and T cells, we conducted CommPath analysis. We performed signaling pathway activity analysis for all cell types (Fig. 9A). The results showed that different cell types exhibited differential activation states in multiple KEGG pathways, suggesting that each cell population might be involved in different biological processes or responses. Subsequently, by constructing a global intercellular communication network, we depicted extensive cell interactions between CAPG + Mac and other cell types (Fig. 9B-C). The network diagram showed that CAPG + Mac acted as a sender and receiver of signals, and there were widespread communication connections between it and T cells and other immune cell populations, suggesting its importance in microenvironment signal exchange. Additionally, we focused the analysis on CAPG + Mac as the core signal-sending cell to detail the communication axis between it and the T cell population. Figure 9D showed that CAPG + Mac, as a signal hub, integrated the signals received by its internal activated specific pathways (such as Chemokine signaling pathway, Cytokine-cytokine receptor interaction, etc.), regulated downstream ligands, and thereby regulated downstream T cell subsets, thereby affecting the local immune microenvironment.

We further conducted a spatial co-localization analysis of key LR pairs using spatial transcriptomic data (Fig. 9E). The ligand and receptor genes of APOE-LRP1, IL1RN-IL1R1, CCL5-CCR1, and CCL18-CCR1 showed significant spatial co-expression and interaction intensity in tissue sections. In conclusion, CAPG + Mac, as an important signal hub in the tissue microenvironment, through specific LR-mediated pathways activation, suggests its potential ability to regulate T cell function, thereby affecting the local immune microenvironment.

3.9 A prognostic model based on CAPG + Mac marker genes reveals HCC patient risk stratification and immune microenvironment features

To evaluate the clinical prognostic value of CAPG + Mac, we calculated enrichment scores using CAPG + Mac marker genes in TCGA HCC transcriptomes. Survival analysis showed significantly worse overall survival in the high CAPG + Mac score group

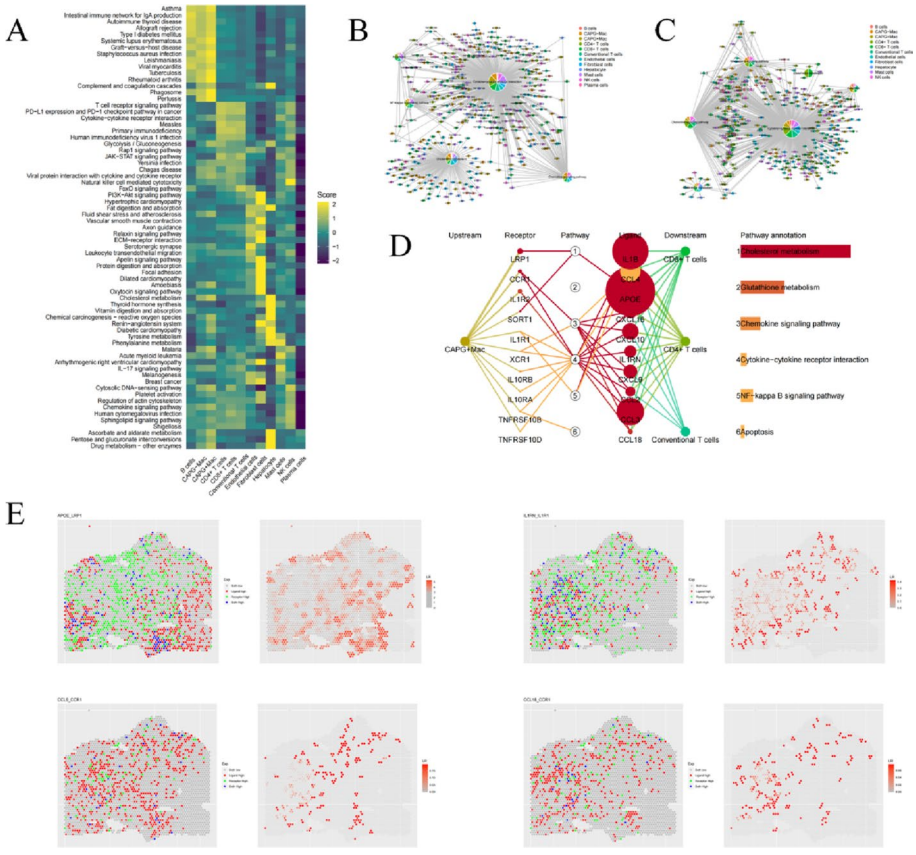

Fig. 9 Cell-cell communication networks and signaling pathways identified by CommPath and verified by SpaGene for ligand-receptor (LR) spatial colocalization. (**A**) The heatmap illustrates the communication pathway intensity across various cell subtypes, specifically highlighting the top 10 upregulated pathways within each cell population. (**B**) The upstream cell communication mode centered on CAPG + Mac. (**C**) The downstream cell communication mode centered on CAPG + Mac. The network diagram converges on the central signaling pathway of CAPG + Mac. The pie charts within the network represent the activated signaling pathways, with the size indicating the total amount of signals received or sent, and the color of the sectors representing the relative contribution proportions of different cell clusters. The adjacent scatter plots show the LR pairs released by the cells and then paired with the receptors in the connection path. (**D**) This network diagram displays CAPG + Mac as a signal sender, outlining six key signaling pathways and their involved LR interactions with CD8+, CD4+, and Conventional T cells. (**E**) The SpaGene analysis revealed the co-expression and interaction intensities of the four key LR pairs in the tissue space (APOE-LRP1, IL1RN-IL1R1, CCL5-CCR1, CCL18-CCR1).

(Fig. 10A). We then performed univariate Cox regression to identify survival-related candidates and applied LASSO with cross-validation to optimize the regularization parameter (lambda) for variable selection (Fig. 10B–D). Using TCGA as the training set, we constructed a multivariate Cox model (Fig. 10E) and externally validated it in the ICGC cohort. Individual risk scores were computed and patients were stratified into high- and low-risk groups by the median. LDHA, ALDH2, SPP1, and TXN were ultimately identified as the core genes constituting the prognostic signature. Model performance assessments showed that Kaplan–Meier curves demonstrated significantly shorter OS in the high-risk group in both training and validation cohorts (Fig. 10F, H). ROC analyses yielded 1/3/5-year AUCs of 0.722/0.711/0.729 in the training set and 0.721/0.714/0.483 in the validation set, indicating overall good predictive capability (Fig. 10G, I). Univariate and multivariate regression (Supplementary Fig. 3A, 3B) further supported the score as an independent prognostic factor. The immunohistochemical results based on the HPA database showed that when comparing healthy liver tissue with liver cancer tissue, the

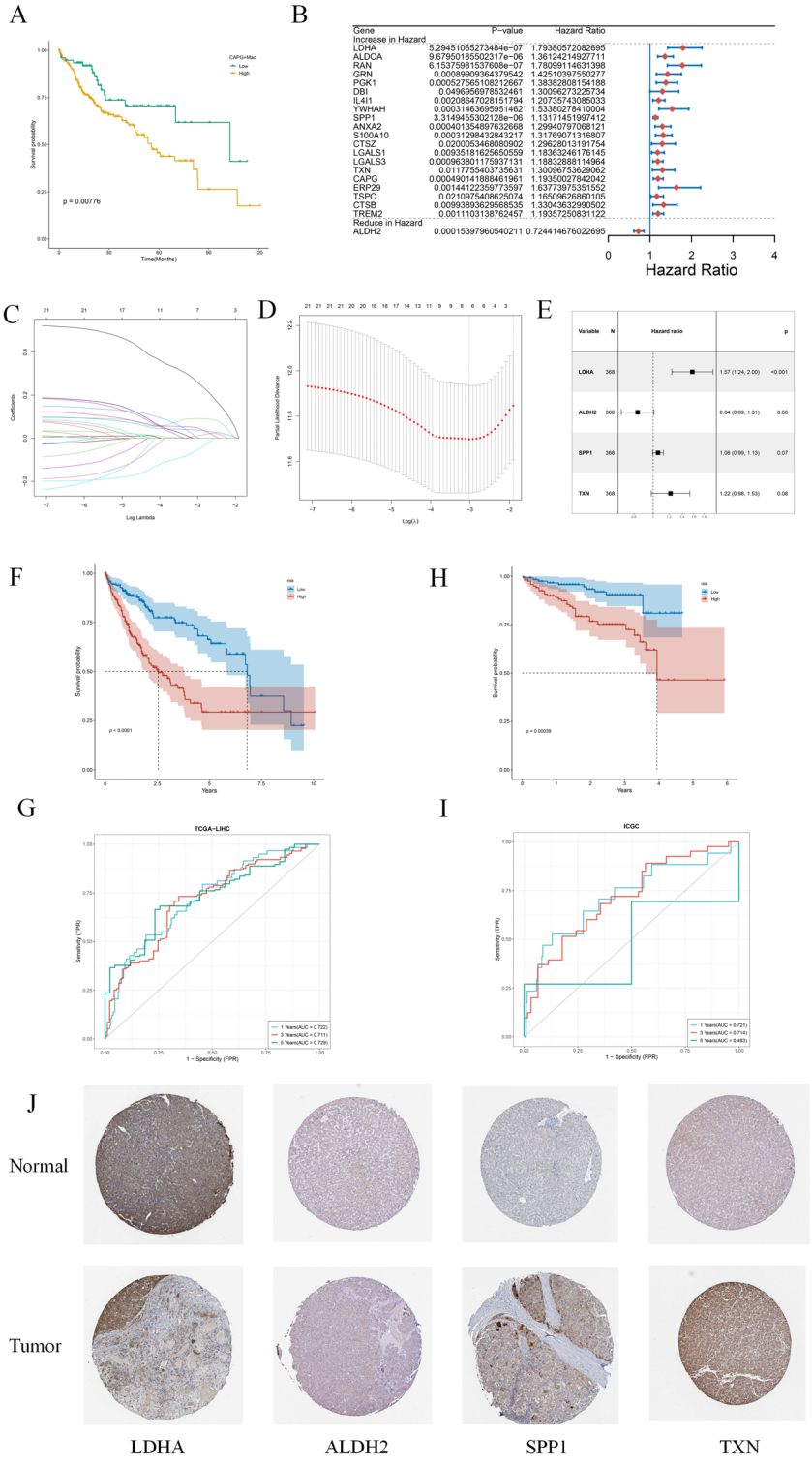

Fig. 10 Construction and validation of a prognostic model based on CAPG + Mac marker genes in HCC. (**A**) Kaplan–Meier survival curves comparing overall survival between high- and low-CAPG$^+$ macrophage enrichment score groups. (**B**) Univariate Cox regression analysis identifying prognosis-related genes among CAPG$^+$ macrophage markers. (**C–D**) LASSO regression and cross-validation plots used to select optimal prognostic genes. (**E**) Multivariate Cox regression analysis identifying independent prognostic markers, which were subsequently used to construct the prognostic model. (**F–G**) Kaplan–Meier and ROC curves showing the predictive performance of the model in the TCGA-LIHC cohort. (**H–I**) Kaplan–Meier and ROC validation curves confirming model robustness in the independent ICGC cohort. (**J**) Protein expression of LDHA, ALDH2, SPP1, and TXN in HCC and normal liver tissues.

protein expressions of SPP1 and TXN in the tumors increased, while there were no significant differences in LDHA and ALDH2 (Fig. 10J).

To elucidate associations between the risk score and the immune microenvironment, we evaluated immune infiltration and composition. Compared with the low-risk group, the high-risk group exhibited more abundant immune cell infiltration (Supplementary Fig. 4A), with significantly higher immune scores, ESTIMATE scores, and tumor purity (Supplementary Fig. 4B). Activities across all stages of tumor-infiltrating immune cell (TIIC)–related pathways were synchronously upregulated in the high-risk group (Supplementary Fig. 4C), suggesting that higher risk scores are associated with a more active immune milieu. Notably, multiple immune checkpoint genes were significantly upregulated in the high-risk group (Supplementary Fig. 4D), a pattern that may suppress effector responses and facilitate immune escape, thereby contributing to poor prognosis under an immune-active yet functionally constrained context. Subsequently, we included multiple immunotherapy cohorts and evaluated the prognostic value of these risk scores. The low-risk score showed better prognosis in the post-immunotherapy population (GSE78220, $p = 0.042$, Supplementary Fig. 4E; GSE135222, $p = 0.0013$, Supplementary Fig. 4F). The low-risk score is usually associated with a better outcome of immunotherapy (GSE91061, $p = 0.0091$; Supplementary Fig. 4G).

4 Discussion

We integrated multidimensional transcriptomic data anchored on ferroptosis-related genes to identify FIMRGs closely associated with the immune microenvironment and systematically characterized, at single-cell resolution, their impact on the HCC immune milieu. We observed a marked upregulation of FIMRG-related scores in macrophages. Within the HCC microenvironment, ferroptosis–immune signaling appears to regulate macrophage activation states and spatial distribution. Further analyses prioritized CAPG as a core candidate, suggesting a potential key role in tumor immune regulation. Leveraging multi-omics evidence, we delineated the spatial features of CAPG + Mac, its immune communication networks, its potential influence on T cell exhaustion, and its utility in prognostic assessment and immune response. Together, our findings support the hypothesis that CAPG may promote tumor progression by inhibiting macrophage ferroptosis and fostering T cell exhaustion.

Ferroptosis is receiving growing attention as a therapeutic target in oncology. Multiple strategies—including radiotherapy, chemotherapy, and immunotherapy—can impede tumor progression by inducing ferroptosis [47, 48]. Induction of ferroptosis can enhance tumor immunogenicity and promote T cell infiltration, while resensitizing resistant cancer cells to immune checkpoint inhibitors, CAR-T cell therapy, and monoclonal antibodies. Targeting ferroptosis pathways may also disrupt immune evasion mediated by regulatory T cells and myeloid-derived suppressor cells (MDSCs), thereby improving immunotherapy efficacy [49]. In HCC, high DUSP4 expression has been linked to sorafenib resistance, underscoring the potential value of ferroptosis-targeted interventions [50]. Our study detected a significant elevation of glutathione (GSH) metabolism during HCC progression, consistent with evidence implicating the oxidative stress–ARD1–PABPC1–GCLC axis in GSH metabolic reprogramming and ferroptosis regulation in HCC [51]. Moreover, NRF2 signaling can upregulate key GSH-synthesis enzymes such as SLC7A11 and GCLC, enhancing macrophage antioxidant defenses and

resistance to ferroptosis [52], highlighting the centrality of GSH in HCC. Recent mechanistic work has further strengthened this view. Zhang et al. demonstrated that CAPG directly suppresses ferroptosis through the WDR74-p53-SLC7A11 signaling axis, promoting glutathione synthesis, tumor cell proliferation, and sorafenib resistance in HCC [53]. This mechanistic link between CAPG and ferroptosis inhibition provides strong biological support for our single-cell findings that CAPG + Mac may acquire enhanced antioxidant capacity and resist ferroptotic cell death, thereby maintaining an immunosuppressive phenotype within the tumor microenvironment. TAMs, a major TME component, are commonly associated with poor prognosis and therapeutic resistance, including to immunotherapy. M2 polarization of TAMs promotes immunosuppression and immune escape, and is shaped by metabolism, epigenetics, transcriptional regulation, and signaling pathways [54]. Accordingly, targeting TAMs and repolarization strategies are promising therapeutic approaches [55]. For example, LSCC-sEVs can drive metabolic reprogramming of TAMs toward an M2 phenotype and impair CD8 + T cell function, accelerating tumor progression [56]. Macrophages can also deliver PRDX6 to bypass GPX4 inhibition, thereby limiting GPX4-related ferroptosis in cancer cells, collectively illustrating the substantial impact of macrophages in the TME [57].

Historically, CAPG has been studied as a regulator of actin elongation in cancer metastasis [58]. As a ferroptosis-related gene, CAPG expression can influence immune cell infiltration and TME homeostasis, playing an important role in immune regulation in uterine corpus endometrial carcinoma [59]. High CAPG levels correlate with shorter relapse-free survival and hyperactive PI3K/Akt signaling in breast cancer, indicating poor response to paclitaxel [60]. CAPG also signals through the Wnt/β-catenin pathway in gastric cancer [61]. Members of the gelsolin superfamily, including CAPG, may modulate the balance between protumor and antitumor immunity in endometrial cancer, contributing to an immunosuppressive TME and T cell exhaustion [62]. Although CAPG has been linked to HCC [63], its mechanistic role in HCC remains unclear. Beyond these specific mechanisms, the intricate regulation of gene expression by RNA binding proteins (RBPs) is increasingly recognized as a critical determinant in shaping the complex immune microenvironment and promoting immune evasion in various cancers, including HCC [64 65]. Multiple studies nonetheless suggest therapeutic relevance: CAPG can inhibit cell death and ferroptosis while promoting Colorectal Cancer (CRC) proliferation via suppression of the P53 pathway, pointing to a potential CRC target [66]. In glioma, circ_0055412 promotes cisplatin resistance by stabilizing CAPG mRNA and modulating Wnt/β-catenin signaling [67]. Additionally, upon p70S6K1 downregulation/blockade, GA-induced upregulation of cancer-associated proteins (including enolase-2, capping protein CAPG, galectin-3, and cathepsin D) was suppressed, exerting therapeutic effects in glycated albumin–induced triple-negative breast cancer [68]. Our work is the first to suggest that CAPG + Mac may modulate the HCC TME by promoting T cell exhaustion, highlighting CAPG as a potential target to enhance cancer immunotherapy. Moreover, experimental evidence indicates that macrophages can deplete T cells using mouse mATG [69], supporting our observations. We therefore hypothesize that CAPG may enhance glutathione and related metabolic pathways to suppress macrophage ferroptosis and maintain their immunosuppressive state. This could hinder the recruitment and functional activation of effector T cells and promote T cell exhaustion, thereby driving immune escape. Further analyses show that patients with CAPG + Mac often display

higher immune activity and elevated checkpoint expression yet paradoxically have worse prognosis. Prior studies similarly associate high CAPG expression with poor outcomes in certain cancers [70, 71], and TAMs can promote immunosuppression and tumor progression by regulating cytoskeletal dynamics and inflammatory signaling [72]. TAM-specific genes have been validated as predictors of survival and therapeutic responses [73,74]. Immune checkpoint inhibitors (ICIs) are pivotal in cancer immunotherapy; by blocking checkpoint–ligand interactions, immune activity can be restored and tumor clearance enhanced [75]. Notably, HCC patients with higher immune checkpoint burden tend to have poorer prognosis and fewer activated CD8 + T cells [76]. Based on these observations, we posit that although the high-risk group exhibits abundant immune infiltration, immune functions may be impaired, allowing tumor cells to evade surveillance and cytotoxicity and resulting in worse outcomes. Incorporating CAPG + Mac into composite predictive models may help reflect tumor immune status, stratify risk, and guide individualized therapy, thereby offering a novel molecular target and risk assessment strategy for precision immunotherapy. As research on TAM–tumor interactions expands, unique TAM features during malignant progression have been delineated. For instance, Li et al. recently provided an impressive high-resolution atlas of HCC TAMs, uncovering specific subsets like CXCL10 + macrophages with distinct clinical relevance. Such findings underscore the value of TAMs in early prediction, intervention, and prognostication [77, 78]. For instance, Umiker et al. developed JTX-8064, a selective antagonistic monoclonal antibody that blocks LILRB2–ligand binding, reprograms human TAMs, and drives intratumoral T cell activation [79]. In most solid tumors, high macrophage density is associated with poor prognosis. CD163, a TAM receptor, plays a critical role in tumor progression; its differential expression and association with adverse prognosis have been reported in colorectal cancer [80]. Our study is the first to systematically reveal the key role of CAPG + Mac in the TME, expanding understanding of CAPG's functions in tumorigenesis and progression, and providing avenues for precise TAM-targeted interventions. By linking CAPG + Mac with ferroptosis regulation, this study opens promising directions and translational opportunities for ferroptosis-related targeted therapy in HCC.

Despite our comprehensive multi-omics analysis, we acknowledge certain limitations. First, while spatial transcriptomics indicated a close spatial proximity between CAPG+ macrophages and T cells, confirming this physical contact and protein expression via immunohistochemistry (IHC) or immunofluorescence (IF) in clinical samples remains necessary to corroborate the predicted ligand–receptor crosstalk. Second, although we identified specific metabolic features like enhanced glutathione metabolism, the precise molecular machinery—spanning iron metabolism, ROS dynamics, and antigen presentation—warrants further experimental validation. Our follow-up studies will integrate in vivo models and in vitro assays to rigorously elucidate these mechanisms and validate their clinical utility

Supplementary Information

The online version contains supplementary material available at https://doi.org/10.1007/s12672-026-04649-2.

Supplementary Material 1

Acknowledgements
Not applicable.

Author contributions
Xisheng Yin - Methodology, Formal Analysis, Writing Review & Editing, Yantong Li-Conceptualization, Methodology, Investigation, Writing Original Draft, Software, Validation, Data Curation, Shi Zheng – Supervision, Methodology, Writing – Review & Editing, Chunhui Pan – Data Curation, Visualization, Validation, Zihan Tian –Software, Investigation, Xiaolin Zhong- Resources, Project Administration, Funding Acquisition.

Funding
This study was funded by the Sichuan Medical Science and Technology Innovation Research Association Project YCH-KY-YCZD2024-298; Beijing Huaxia Cancer Prevention and Treatment Research Institute Project 202401.

Data availability
Publicly available datasets analyzed in this study include: scRNA-seq (GSE162631), spatial transcriptomics (GSE224411), and immunotherapy cohorts (GSE78220, GSE135222, GSE91061), all accessible via GEO (https://www.ncbi.nlm.nih.gov/geo/). Bulk RNA-seq data were obtained from TCGA (https://portal.gdc.cancer.gov/) and ICGC (https://dcc.icgc.org/). Further data and code are available from the corresponding author upon reasonable request.

Declarations

Ethics approval and consent to participate
Not applicable.

Consent for publication
Not applicable.

Competing interests
The authors declare no competing interests.

Received: 24 November 2025 / Accepted: 9 February 2026
Published online: 22 February 2026

References

1. Karsidag I, Liu H. The recent changing global landscape of cancer. Life Conflux. 2025;2(1):e312. https://doi.org/10.71321/e37ss652.
2. Zhu GQ, Tang Z, Huang R, et al. CD36 + cancer-associated fibroblasts provide immunosuppressive microenvironment for hepatocellular carcinoma via secretion of macrophage migration inhibitory factor. Cell Discov. 2023;9(1):25. https://doi.org/10.1038/s41421-023-00529-z.
3. Sangro B, Sarobe P, Hervás-Stubbs S, Melero I. Advances in immunotherapy for hepatocellular carcinoma. Nat Rev Gastroenterol Hepatol. 2021;18(8):525–43. https://doi.org/10.1038/s41575-021-00438-0.
4. Hong F, Meng Q, Zhang W, et al. Single-Cell analysis of the Pan-Cancer immune microenvironment and sctime portal. Cancer Immunol Res. 2021;9(8):939–51. https://doi.org/10.1158/2326-6066.CIR-20-1026.
5. Zhao L, Zhou X, Xie F, et al. Ferroptosis in cancer and cancer immunotherapy. Cancer Commun. 2022;42(2):88–116. https://doi.org/10.1002/cac2.12250.
6. Imai H, Nakagawa Y. Biological significance of phospholipid hydroperoxide glutathione peroxidase (PHGPx, GPx4) in mammalian cells. Free Radic Biol Med. 2003;34(2):145–69. https://doi.org/10.1016/s0891-5849(02)01197-8.
7. Lei G, Zhuang L, Gan B. The roles of ferroptosis in cancer: tumor suppression, tumor microenvironment, and therapeutic interventions. Cancer Cell. 2024;42(4):513–34. https://doi.org/10.1016/j.ccell.2024.03.011.
8. Yang M, Cui W, Lv X, et al. S100P is a ferroptosis suppressor to facilitate hepatocellular carcinoma development by rewiring lipid metabolism. Nat Commun. 2025;16:509. https://doi.org/10.1038/s41467-024-55785-8.
9. Wang Y, Hu J, Wu S, et al. Targeting epigenetic and posttranslational modifications regulating ferroptosis for the treatment of diseases. Signal Transduct Target Ther. 2023;8:449. https://doi.org/10.1038/s41392-023-01720-0.
10. Tang B, Zhu J, Wang Y, et al. Targeted xCT-mediated ferroptosis and protumoral polarization of macrophages is effective against HCC and enhances the efficacy of the anti-PD-1/L1 response. Adv Sci. 2022;10(2):2203973. https://doi.org/10.1002/advs.202203973.
11. Wang W, Green M, Choi JE, et al. CD8 + T cells regulate tumour ferroptosis during cancer immunotherapy. Nature. 2019;569(7755):270–4. https://doi.org/10.1038/s41586-019-1170-y.
12. Lei G, Zhuang L, Gan B. Targeting ferroptosis as a vulnerability in cancer. Nat Rev Cancer. 2022;22(7):381–96. https://doi.org/10.1038/s41568-022-00459-0.
13. Xia Y, Rao L, Yao H, Wang Z, Ning P, Chen X. Engineering macrophages for cancer immunotherapy and drug delivery. Adv Mater Deerfield Beach Fla. 2020;32(40):e2002054. https://doi.org/10.1002/adma.202002054.
14. Kapralov AA, Yang Q, Dar HH, et al. Redox lipid reprogramming commands susceptibility of macrophages and microglia to ferroptotic death. Nat Chem Biol. 2020;16(3):278–90. https://doi.org/10.1038/s41589-019-0462-8.
15. Xu C, Sun S, Johnson T, et al. The glutathione peroxidase Gpx4 prevents lipid peroxidation and ferroptosis to sustain Treg cell activation and suppression of antitumor immunity. Cell Rep. 2021;35(11):109235. https://doi.org/10.1016/j.celrep.2021.109235.
16. Smyth GK. Linear models and empirical Bayes methods for assessing differential expression in microarray experiments. Stat Appl Genet Mol Biol. 2004;3(Article3). https://doi.org/10.2202/1544-6115.1027.
17. Wilkerson MD, Hayes DN. ConsensusClusterPlus: a class discovery tool with confidence assessments and item tracking. Bioinforma Oxf Engl. 2010;26(12):1572–3. https://doi.org/10.1093/bioinformatics/btq170.
18. Jia Q, Wu W, Wang Y, et al. Local mutational diversity drives intratumoral immune heterogeneity in non-small cell lung cancer. Nat Commun. 2018;9(1):5361. https://doi.org/10.1038/s41467-018-07767-w.

19. Langfelder P, Horvath S. WGCNA: an R package for weighted correlation network analysis. BMC Bioinformatics. 2008;9:559. https://doi.org/10.1186/1471-2105-9-559.
20. Korsunsky I, Millard N, Fan J, et al. Fast, sensitive and accurate integration of single-cell data with harmony. Nat Methods. 2019;16(12):1289–96. https://doi.org/10.1038/s41592-019-0619-0.
21. Jin S, Guerrero-Juarez CF, Zhang L, et al. Inference and analysis of cell-cell communication using cellchat. Nat Commun. 2021;12(1):1088. https://doi.org/10.1038/s41467-021-21246-9.
22. Zhang F, Li X, Tian W. Unsupervised inference of developmental directions for single cells using VECTOR. Cell Rep. 2020;32(8):108069. https://doi.org/10.1016/j.celrep.2020.108069.
23. Pham D, Tan X, Balderson B, et al. Robust mapping of Spatiotemporal trajectories and cell-cell interactions in healthy and diseased tissues. Nat Commun. 2023;14(1):7739. https://doi.org/10.1038/s41467-023-43120-6.
24. Cable DM, Murray E, Zou LS, et al. Robust decomposition of cell type mixtures in Spatial transcriptomics. Nat Biotechnol. 2022;40(4):517–26. https://doi.org/10.1038/s41587-021-00830-w.
25. Tanevski J, Flores ROR, Gabor A, Schapiro D, Saez-Rodriguez J. Explainable multiview framework for dissecting Spatial relationships from highly multiplexed data. Genome Biol. 2022;23(1):97. https://doi.org/10.1186/s13059-022-02663-5.
26. Salié H, Wischer L, D'Alessio A, et al. Spatial single-cell profiling and neighbourhood analysis reveal the determinants of immune architecture connected to checkpoint inhibitor therapy outcome in hepatocellular carcinoma. Gut. 2025;74(3):451–66. https://doi.org/10.1136/gutjnl-2024-332837.
27. Lu H, Ping J, Zhou G, et al. CommPath: an R package for inference and analysis of pathway-mediated cell-cell communication chain from single-cell transcriptomics. Comput Struct Biotechnol J. 2022;20:5978–83. https://doi.org/10.1016/j.csbj.2022.10.028.
28. Liu Q, Hsu CY, Shyr Y. Scalable and model-free detection of Spatial patterns and colocalization. Genome Res. 2022;32(9):1736–45. https://doi.org/10.1101/gr.276851.122.
29. Hugo W, Zaretsky JM, Sun L, et al. Genomic and transcriptomic features of response to anti-PD-1 therapy in metastatic melanoma. Cell. 2016;165(1):35–44. https://doi.org/10.1016/j.cell.2016.02.065.
30. Jung H, Kim HS, Kim JY, et al. DNA methylation loss promotes immune evasion of tumours with high mutation and copy number load. Nat Commun. 2019;10(1):4278. https://doi.org/10.1038/s41467-019-12159-9.
31. Harjunpää H, Llort Asens M, Guenther C, Fagerholm SC. Cell adhesion molecules and their roles and regulation in the immune and tumor microenvironment. Front Immunol. 2019;10:1078. https://doi.org/10.3389/fimmu.2019.01078.
32. Jo Y, Sim HI, Yun B, Park Y, Jin HS. Revisiting T-cell adhesion molecules as potential targets for cancer immunotherapy: CD226 and CD2. Exp Mol Med. 2024;56(10):2113–26. https://doi.org/10.1038/s12276-024-01317-9.
33. Zhou T, Qian H, Zhang D, et al. PGRN inhibits CD8 + T cell recruitment and promotes breast cancer progression by up-regulating ICAM-1 on TAM. Cancer Immunol Immunother CII. 2024;73(5):76. https://doi.org/10.1007/s00262-024-03655-z.
34. Croft M. The TNF family in T cell differentiation and function–unanswered questions and future directions. Semin Immunol. 2014;26(3):183–90. https://doi.org/10.1016/j.smim.2014.02.005.
35. Gottschlich A, Grünmeier R, Hoffmann GV, et al. Dissection of single-cell landscapes for the development of chimeric antigen receptor T cells in hodgkin lymphoma. Blood. 2025;145(14):1536–52. https://doi.org/10.1182/blood.2023022197.
36. Llaó-Cid L, Wong J, Fernandez Botana I, et al. Integrative multi-omics reveals a regulatory and exhausted T-cell landscape in CLL and identifies galectin-9 as an immunotherapy target. Nat Commun. 2025;16(1):7271. https://doi.org/10.1038/s41467-025-61822-x.
37. Yang R, Sun L, Li CF, et al. Galectin-9 interacts with PD-1 and TIM-3 to regulate T cell death and is a target for cancer immunotherapy. Nat Commun. 2021;12(1):832. https://doi.org/10.1038/s41467-021-21099-2.
38. Li D, Liu J, Yu L, Luo X, Wu X, Chen R. Integrated Single-Cell RNA-Seq reveals immunosuppressive mechanisms of Treg cell differentiation and tumor microenvironment interactions in colorectal cancer. Cancer Med. 2025;14(17):e71202. https://doi.org/10.1002/cam4.71202.
39. Chen C, Cai Y, Hu W, et al. Single-cell eQTL mapping reveals cell Subtype-specific genetic control and mechanism in malignant transformation of colorectal cancer. Cancer Discov. 2025;15(8):1649–75. https://doi.org/10.1158/2159-8290.CD-24-1561.
40. Jiang P, Gu S, Pan D, et al. Signatures of T cell dysfunction and exclusion predict cancer immunotherapy response. Nat Med. 2018;24(10):1550–8. https://doi.org/10.1038/s41591-018-0136-1.
41. Salomé B, Sfakianos JP, Ranti D, et al. NKG2A and HLA-E define an alternative immune checkpoint axis in bladder cancer. Cancer Cell. 2022;40(9):1027–e10439. https://doi.org/10.1016/j.ccell.2022.08.005.
42. Sun Y, Wu P, Zhang Z, et al. Integrated multi-omics profiling to dissect the Spatiotemporal evolution of metastatic hepatocellular carcinoma. Cancer Cell. 2024;42(1):135–e15617. https://doi.org/10.1016/j.ccell.2023.11.010.
43. Chang JQ, Guo Y, Yuan WJ, et al. HLA-DR$^+$ tumor cells show an association with a distinct immune microenvironment and CD8$^+$ T-Cell exhaustion in HBV-Associated hepatocellular carcinoma. Adv Sci Weinh Baden-Wurtt Ger. 2025;12(30):e02979. https://doi.org/10.1002/advs.202502979.
44. Wermke M, Araujo DM, Chatterjee M, et al. Autologous T cell therapy for PRAME+ advanced solid tumors in HLA-A*02 + patients: a phase 1 trial. Nat Med. 2025;31(7):2365–74. https://doi.org/10.1038/s41591-025-03650-6.
45. Restelli C, Ruella M, Paruzzo L, Tarella C, Pelicci PG, Colombo E. Recent advances in Immune-Based therapies for acute myeloid leukemia. Blood Cancer Discov. 2024;5(4):234–48. https://doi.org/10.1158/2643-3230.BCD-23-0202.
46. Witt M, Oliveira-Ferrer L, Koch-Nolte F, et al. Expression of CD39 is associated with T cell exhaustion in ovarian cancer and its Blockade reverts T cell dysfunction. Oncoimmunology. 2024;13(1):2346359. https://doi.org/10.1080/2162402X.2024.2346359.
47. Zhou Q, Meng Y, Li D, et al. Ferroptosis in cancer: from molecular mechanisms to therapeutic strategies. Signal Transduct Target Ther. 2024;9(1):55. https://doi.org/10.1038/s41392-024-01769-5.
48. Lei G, Zhang Y, Koppula P, et al. The role of ferroptosis in ionizing radiation-induced cell death and tumor suppression. Cell Res. 2020;30(2):146–62. https://doi.org/10.1038/s41422-019-0263-3.
49. Ebrahimnezhad M, Valizadeh A, Yousefi B. Ferroptosis and immunotherapy: breaking barriers in cancer treatment resistance. Crit Rev Oncol Hematol. 2025;214:104907. https://doi.org/10.1016/j.critrevonc.2025.104907.
50. Hao SH, Ma XD, Xu L, et al. Dual specific phosphatase 4 suppresses ferroptosis and enhances Sorafenib resistance in hepatocellular carcinoma. Drug Resist Updat Rev Comment Antimicrob Anticancer Chemother. 2024;73:101052. https://doi.org/10.1016/j.drup.2024.101052.

51. Liu Y, Liu FS, Liu J, et al. The acetyltransferase ARD1 induces glutathione synthesis to facilitate ferroptosis evasion in hepatocellular carcinoma. Cancer Res. 2025;21. https://doi.org/10.1158/0008-5472.CAN-24-4015.
52. Li Q, Yang X, Li T. Natural flavonoids from herbs and nutraceuticals as ferroptosis inhibitors in central nervous system diseases: current preclinical evidence and future perspectives. Front Pharmacol. 2025;16:1570069. https://doi.org/10.3389/fphar.2025.1570069.
53. Quan B, Yao F, Liu W, et al. Increased CAPG inhibits ferroptosis to drive tumor proliferation and Sorafenib resistance in hepatocellular carcinoma via the WDR74-p53-SLC7A11 pathway. Int J Biol Sci. 2025;21(12):5476–95. https://doi.org/10.7150/ijbs.111419.
54. Hu Y, Tang J, Sun H, et al. Artesunate modulates the tumor microenvironment via STAT1/IRF1-mediated TAM repolarization and T cell activation in non-small cell lung cancer. Phytomedicine Int J Phytother Phytopharm. 2025;146:157085. https://doi.org/10.1016/j.phymed.2025.157085.
55. Xiang X, Wang J, Lu D, Xu X. Targeting tumor-associated macrophages to synergize tumor immunotherapy. Signal Transduct Target Ther. 2021;6(1):75. https://doi.org/10.1038/s41392-021-00484-9.
56. Chen X, Zhao Z, Zhao R, et al. STC1 encapsulated in small extracellular vesicles from laryngeal squamous cell carcinoma cells induces CD8 + T cell dysfunction by reprogramming tumor-associated macrophages into M2-like macrophages. Cancer Immunol Immunother CII. 2025;74(2):64. https://doi.org/10.1007/s00262-024-03915-y.
57. Zheng N, Li F, Huang Q, Huang X, Maj T. Macrophages and macrophage extracellular vesicles confer cancer ferroptosis resistance via PRDX6-mediated mitophagy Inhibition. Redox Biol. 2025;86:103826. https://doi.org/10.1016/j.redox.2025.103826.
58. Yun DP, Wang YQ, Meng DL, et al. Actin-capping protein CapG is associated with prognosis, proliferation and metastasis in human glioma. Oncol Rep. 2018;39(3):1011–22. https://doi.org/10.3892/or.2018.6225.
59. Liu J, Zhu W, Xia L, et al. Identification of CAPG as a potential prognostic biomarker associated with immune cell infiltration and ferroptosis in uterine corpus endometrial carcinoma. Front Endocrinol. 2024;15:1452219. https://doi.org/10.3389/fendo.2024.1452219.
60. Chi Y, Xue J, Huang S, et al. CapG promotes resistance to Paclitaxel in breast cancer through transactivation of PIK3R1/P50. Theranostics. 2019;9(23):6840–55. https://doi.org/10.7150/thno.36338.
61. Long Y, Wu J, Shen Y, et al. CAPG is a novel biomarker for early gastric cancer and is involved in the Wnt/β-catenin signaling pathway. Cell Death Discov. 2024;10(1):15. https://doi.org/10.1038/s41420-023-01767-6.
62. Jiang S, Ye M, Wan J, et al. Significance of Gelsolin superfamily genes in Diagnosis, prognosis and immune microenvironment regulation for endometrial cancer. Cancer Med. 2025;14(4):e70584. https://doi.org/10.1002/cam4.70584.
63. Zhou Q, Tao C, Ge Y, et al. A novel single-cell model reveals ferroptosis-associated biomarkers for individualized therapy and prognostic prediction in hepatocellular carcinoma. BMC Biol. 2024;22(1):133. https://doi.org/10.1186/s12915-024-01931-z.
64. Han H, Yuan Y, Li C, et al. RNA-binding motif protein 28 enhances angiogenesis by improving STAT3 translation in hepatocellular carcinoma. Cancer Lett. 2024;604:217191. https://doi.org/10.1016/j.canlet.2024.217191.
65. Han H, Shi Q, Zhang Y, et al. RBM12 drives PD-L1-mediated immune evasion in hepatocellular carcinoma by increasing JAK1 mRNA translation. Oncogene. 2024;43(41):3062–77. https://doi.org/10.1038/s41388-024-03140-y.
66. Zhao Y, Ma R, Wang C, et al. CAPG interference induces apoptosis and ferroptosis in colorectal cancer cells through the P53 pathway. Mol Cell Probes. 2023;71:101919. https://doi.org/10.1016/j.mcp.2023.101919.
67. Zhou Q, Fu Q, Shaya M, Kugeluke Y, Li S, Dilimulati Y. Knockdown of circ_0055412 promotes cisplatin sensitivity of glioma cells through modulation of CAPG and Wnt/β-catenin signaling pathway. CNS Neurosci Ther. 2022;28(6):884–96. https://doi.org/10.1111/cns.13820.
68. Alanazi F, Alsaleh AA, Alamoudi MK, Alasiri A, Haymond A, Matou-Nasri S. Targeting p70S6K1 inhibits glycated Albumin-Induced Triple-Negative breast cancer cell invasion and overexpression of Galectin-3, a potential prognostic marker in diabetic patients with invasive breast cancer. Biomedicines. 2025;13(3):612. https://doi.org/10.3390/biomedicines13030612.
69. Neff KS, Richards SM, Williams JM, Garman RD, Ruzek MC. Murine antithymocyte Globulin T-cell depletion is mediated predominantly by macrophages, but the Fas/FasL pathway selectively targets regulatory T cells. Transplantation. 2011;92(5):523–8. https://doi.org/10.1097/TP.0b013e31822923f7.
70. Lang Z, Chen Y, Zhu H, et al. Prognostic and clinicopathological significance of CapG in various cancers: evidence from a meta-analysis. Pathol Res Pract. 2019;215(12):152683. https://doi.org/10.1016/j.prp.2019.152683.
71. Liu W, Yin H, Xie Z, et al. FYB1-targeted modulation of CAPG promotes AML progression. Mol Cell Biochem. 2025;480(2):985–99. https://doi.org/10.1007/s11010-024-04992-4.
72. Fu Q, Shaya M, Li S, et al. Analysis of clinical characteristics of macrophage capping protein (CAPG) gene expressed in glioma based on TCGA data and clinical experiments. Oncol Lett. 2019;18(2):1344–50. https://doi.org/10.3892/ol.2019.10396.
73. Hong SM, Lee AY, Kim BJ, et al. NAMPT-Driven M2 polarization of Tumor-Associated macrophages leads to an immunosuppressive microenvironment in colorectal cancer. Adv Sci Weinh Baden-Wurtt Ger. 2024;11(14):e2303177. https://doi.org/10.1002/advs.202303177.
74. Gutiérrez-Seijo A, García-Martínez E, Barrio-Alonso C, et al. CCL20/TNF/VEGFA cytokine secretory phenotype of Tumor-Associated macrophages is a negative prognostic factor in cutaneous melanoma. Cancers. 2021;13(16):3943. https://doi.org/10.3390/cancers13163943.
75. Bagchi S, Yuan R, Engleman EG. Immune checkpoint inhibitors for the treatment of cancer: clinical impact and mechanisms of response and resistance. Annu Rev Pathol. 2021;16:223–49. https://doi.org/10.1146/annurev-pathol-042020-042741.
76. Wu D, Liang S, Guo H, et al. Downregulation of MARC2 promotes immune escape and is associated with immunosuppression of hepatocellular carcinoma. Front Genet. 2021;12:790093. https://doi.org/10.3389/fgene.2021.790093.
77. Xu J, Ding L, Mei J, et al. Dual roles and therapeutic targeting of tumor-associated macrophages in tumor microenvironments. Signal Transduct Target Ther. 2025;10(1):268. https://doi.org/10.1038/s41392-025-02325-5.
78. Li X, Li R, Miao X, et al. Integrated single cell analysis reveals an atlas of tumor associated macrophages in hepatocellular carcinoma. Inflammation. 2024;47(6):2077–93. https://doi.org/10.1007/s10753-024-02026-1.
79. Umiker B, Hashambhoy-Ramsay Y, Smith J, et al. Inhibition of LILRB2 by a novel blocking antibody designed to reprogram immunosuppressive macrophages to drive T-Cell activation in tumors. Mol Cancer Ther. 2023;22(4):471–84. https://doi.org/10.1158/1535-7163.MCT-22-0351.

80. Ma S, Zhao Y, Liu X, et al. CD163 as a potential biomarker in colorectal cancer for tumor microenvironment and cancer prognosis: A Swedish study from tissue microarrays to big data analyses. Cancers. 2022;14(24):6166. https://doi.org/10.3390/cancers14246166.

Publisher's note